

Instrument Science Report COS 2010-09(v1)

# COS FUV External Spectroscopic Performance

---

Parviz Ghavamian<sup>1</sup>, Cynthia Froning<sup>2</sup>, Steven Osterman<sup>2</sup>, Charles D. Keyes<sup>1</sup>, and Dave Sahnou<sup>3</sup>

<sup>1</sup> Space Telescope Science Institute, Baltimore, MD

<sup>2</sup> University of Colorado, Boulder, CO

<sup>3</sup> Johns Hopkins University, Baltimore, MD

30 September 2010

---

## ABSTRACT

*We have performed an analysis of the spectral and spatial resolution of the Cosmic Origins Spectrograph (COS) in its far-ultraviolet channel using spectra acquired during the SM4 Servicing Mission Observatory Verification (SMOV) and during the Cycle 17 FUV sensitivity monitoring program. As described in ISR 2009-01(v1), our results indicate that the on-orbit FUV spectral resolution is reduced compared to values obtained in ground testing due to the redistribution of light from the core of the line spread function (LSF) into the wings. The wings are caused by mid-frequency wavefront errors (MFWFEs) that are produced by zonal (polishing) errors on the HST OTA. Here we compare the effective resolving power obtained from our models of the COS LSF, for cases where the MFWFEs are included and excluded. The spectral resolving power obtained when MFWFEs are included is 16,000-20,000 for G130M and G160M and 2300-3500 for G140L ( $\lambda > 1250 \text{ \AA}$ ). On the other hand, our analysis of the on-orbit spatial resolution perpendicular to dispersion shows that it depends strongly on both wavelength and central wavelength (CENWAVE) setting. This dependence is primarily caused by the known astigmatism introduced by the COS FUV gratings. Over most of its spectral range, the spatial resolution of the FUV channel (as defined by the full width*

*half maximum of a point source spectrum perpendicular to dispersion) meets or exceeds the values measured in ground testing, for both segments of the detector. Across the full range of CENWAVE settings, we obtain a spatial resolution of 0.5" to 1.8" for the G130M grating, 0.3" - 0.6" for G160M and 0.4" - 2.0" for the G140L grating. The corresponding spatial resolution for the BOA aperture is 0.5" – 1.5" for G130M, 0.4" – 0.9" for G160M and 0.7" – 1.5" for G140L. Note that the real values for these gratings will be ~ 15% larger (i.e., slightly lower spatial resolution than quoted) due to our use of a single component fit to the strongly asymmetric BOA spatial profiles. For both the PSA and BOA spectra we present third- and fourth-order polynomial fits to the widths of the cross-dispersion profile as a function of wavelength, for a range of CENWAVE settings. This allows users to estimate the wavelength dependence of the spatial resolution in the FUV. We also present calculations of the plate scale and aperture throughput curves for the FUV channel with the PSA aperture. Both quantities also meet pre-launch specifications.*

---

## **Contents:**

- Introduction (page 3)
- FUV Spectral Resolution (page 3)
- FUV Spatial Resolution (page 5)
- On-Orbit Characterization of the External Performance (page 5)
- Target Selection (page 5)
- Data Acquisition (page 5)
- Data Analysis (page 6)
- Spatial Resolution Analysis (page 6)
- FUV Plate Scale Analysis (page 7)
- Aperture Throughput Analysis (page 7)
- Results (7)
- Spatial Resolution Results (page 7)
- FUV Plate Scale Results (page 18)
- Aperture Throughput Results (page 20)
- Off-Axis Variation of the FUV Spatial Profile (page 22)
- Summary (page 29)
- Change History for COS ISR 2010-09 (page 29)
- References (page 29)
- Appendix (page 30)

## 1. Introduction

The Cosmic Origins Spectrograph (COS) was installed during the most recent servicing mission of the Hubble Space Telescope (SM4). COS is a slitless spectrograph with a 2.5 arcsecond aperture that is optimized for observations of point sources. It is the most sensitive ultraviolet spectrograph flown on HST to date. With its medium resolution gratings (G130M and G160M, covering 1150 Å – 1800 Å) the FUV channel was designed to reach a spectroscopic resolving power of at least 20,000 (15 km/s) across 80% of its passband (STE-63, 2004). The COS NUV channel was designed to cover the 1750 Å – 3200 Å spectral range at spectroscopic resolving powers in its medium resolution gratings (G185M, G225M, and G285M) of 16,000 to >20,000.

In this ISR we describe the analysis results from our programs executed during Servicing Mission Observatory Verification (SMOV). We utilized data from programs 11489 (“FUV External Spectroscopic Performance Part I”) and 11490 (“FUV External Spectroscopic Performance Part II”) to verify the spectral resolution, plate scale and aperture throughput of the FUV channel on COS. We performed our spatial resolution analysis with observations taken from the Cycle 17 COS sensitivity monitoring program (PID 11897, “FUV Spectroscopic Sensitivity Monitoring”). In addition, we used BOA spectra obtained during another SMOV program, PID 11492 (“FUV Spectroscopic Sensitivity”) to estimate the spatial resolution of BOA spectra. Results for the NUV channel are described in a companion ISR (Béland & Ghavamian; COS ISR 2010-08).

## 2. FUV Spectral Resolution

Servicing Mission Observatory Verification (SMOV) program COS-31 (program ID 11489), “FUV External Spectroscopic Performance – Part 1,” was designed to characterize the on-orbit spectral resolution of the FUV channels. Analysis results from that program were reported by Ghavamian et al. (2009). In that analysis it was found that the line spread function (LSF) of the FUV channel was broader than measured in ground testing and exhibited non-Gaussian wings. The broadening of the LSF is due to mid-frequency wavefront errors (MFWFEs) introduced by zonal (polishing) errors on the primary and secondary mirrors of HST and not included in the ground testing. Optical modeling of the effect (Ghavamian et al. 2009) showed that the power in the non-Gaussian wings is strongest at the shortest wavelengths covered in the FUV channel (~1150 Å), diminishing toward longer wavelengths. A detailed discussion of the COS LSF appears in Ghavamian et al. (2009).

Here we summarize the impact of the MFWFE effect on the spectral resolving power of COS using the modeling results from Ghavamian et al. (2009). The effect of the broadened core and non-Gaussian wings of the LSF is to lower the resolving power of COS from the values predicted during ground testing. In **Figure 1**, we present the modeled resolving power of the FUV gratings for two cases: (1) assuming a Gaussian LSF of FWHM 6.5 pixels, as estimated during ground tests (no MFWFEs from the HST

OTA), and (2) an LSF model including the MFWFEs from the HST OTA. In the latter case the FWHM of the LSF is calculated directly from the profile by taking the width at half the peak (values are listed in Table 1 of Ghavamian et al. 2009). As shown in **Figure 1**, the resolving power of the G130M and G160M gratings are  $\sim 20\%$  lower on-orbit than obtained from the ground tests. The G140L profile is least affected by the MFWFEs, due to the lower dispersion of the G140L grating compared to the M mode gratings. This results in a G140L resolving power close to that predicted from ground tests. However, it should be noted that since the Gaussian and full LSF profiles are different in shape, a direct comparison of the widths of the two profiles can be misleading. The impact of the broad wings in the latter profile can be missed, even if they have identical full width half maxima. Rather, **Figure 1** is useful for observers when making a rough determination of the resolving power necessary to achieve their scientific goals. For more refined estimates, observers can then use the published model LSFs in Ghavamian et al. (2009) to judge in detail whether the resolving power of COS is adequate for meeting their scientific needs.

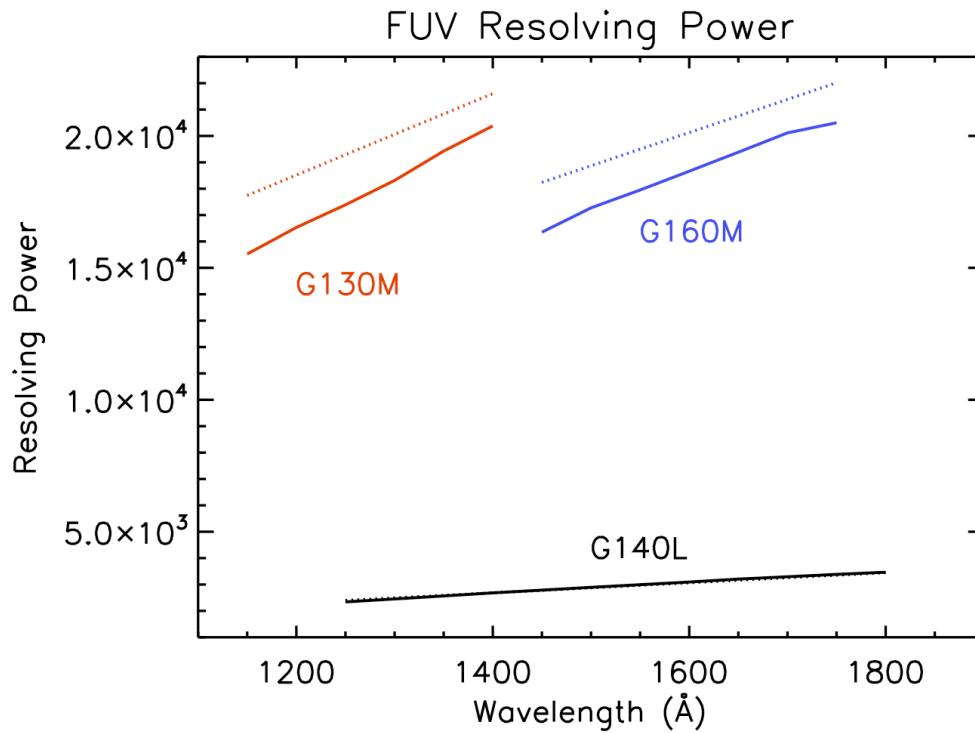


**Figure 1.** The resolving power (defined as  $\lambda/\Delta\lambda_{\text{FWHM}}$ ) for the three gratings of the COS FUV channel as observed through the PSA aperture. The dotted lines are the prelaunch prediction using a Gaussian FWHM of 6.5 pixels. The solid lines are the values predicted by the LSF model with the on-orbit MFWFEs included.

### **3 On-Orbit Characterization of the FUV External Spectroscopic Performance**

After COS was installed on HST, the performance of the spectrograph was tested during the Servicing Mission Observatory Verification (SMOV). The programs used for testing of the spatial resolution, plate scale and aperture throughput are described below.

#### ***3.1 Target Selection***

SMOV program COS-32 (program ID 11490), “FUV External Spectroscopic Performance – Part 2,” was designed to characterize the on-orbit spatial resolution and plate scale of the FUV channels. LIN 358, a point source with emission line spectrum was selected for the PSA observation in this program. LIN358 is a symbiotic star in the Large Magellanic Cloud. It has little or no continuum emission in the FUV but shows several emission lines, including strong emission from the N V  $\lambda\lambda 1238/1242$  and Si IV  $\lambda\lambda 1393/1402$  doublets, OIV]  $\lambda 1398 - \lambda 1402$ , and He II  $\lambda 1640$  (Vogel & Nussbaumer 1995). The emission lines were spectrally unresolved by previous FOS observations but believed to be relatively narrow ( $< 60$  km/s).

While the data from COS-32 were useful for measuring the plate scales and aperture throughput for the FUV gratings, the sparseness of emission lines and faintness of the underlying continua made these sources less useful for characterizing the systematic variations perpendicular to dispersion (and hence spatial resolution) as a function of wavelength. To measure these variations for PSA data, we utilized FUV spectra of two white dwarfs observed as part of the Cycle 17 COS FUV sensitivity monitoring program (PID 11897; R. Osten, PI). In this ongoing program, the white dwarf WD0947+857 is observed monthly with the G130M and G140L gratings, while WD1057+719 is observed monthly with the G160M grating (both stars are HST FASTEX standards). These spectra provide high S/N ( $\sim 30$  per resolution element) continua suitable for measurement of spatial profiles at a range of FUV wavelengths.

We performed a similar spatial profile study for the BOA using data from SMOV program COS-34 (PID 11492, “FUV Spectroscopic Sensitivity”). The target of these observations was the HST flux standard GD71, a white dwarf. The BOA observations were done for all three FUV gratings, but with central wavelength and FPPOS settings aimed to maximize the wavelength range covered by the observations.

#### ***3.2 Data Acquisition***

Spectra of LIN358 were obtained during a single visit on September 14 and 15, 2009 through the PSA with the G130M, G160M, and G140L gratings at the 1309 Å, 1589 Å, and 1230 Å central wavelengths, respectively. The PSA observations were acquired in time-tag mode with tagflash enabled for internal wavelength calibration, while the BOA data were taken in time-tag mode with separate wavecal exposures. To measure the spatial resolution and estimate such quantities as the FUV plate scale and aperture throughput of the PSA, we used the following procedure. First, a spectrum was acquired

at the center of the PSA aperture. Subsequent exposures were then acquired at POSTARG offset positions of 0.25, 0.50, 1.0, 1.50, and 1.75 arcsec along the cross-dispersion axis (+Y). Another exposure was obtained at the center of the aperture and then the star was stepped along the -Y direction, to -0.25, -1.0, -1.50, and -1.75 arcsec. In G160M, the star was also stepped along the dispersion axis, covering +X positions of 0.25, 0.50, 1.0, 1.50, and 1.75 arcsec and -X positions of -0.25, -0.50, -1.0, -1.50, and -1.75 arcsec (all at Y=0).

The PSA spectra of WD0947+857 analyzed here were acquired on April 1, 2010 at central wavelength settings of 1291 Å, 1309 Å and 1327 Å for G130M and 1105 Å and 1230 Å for G140L. The WD1057+719 data were acquired on April 19, 2010 using the G160M grating, with exposures taken at all central wavelength settings (1577, 1589, 1600, 1611 and 1623 Å). All exposures were taken at the nominal FPPOS position of 3. More details of the observational setup can be found in the FUV sensitivity monitoring ISR by R. Osten (COS ISR 2010-15). The BOA spectra of GD71 used in our spatial resolution analysis were acquired on September 15, 2009 (PID 11492). The data files utilized in the PSA and BOA spatial resolution analyses are listed in **Table 1**. The data files used in the plate scale and aperture throughput determination are listed in **Tables 3-5**.

### **3.3 Data Analysis**

We used several of tools to perform our spatial profile analyses, including IDL software contained in the CEDAR package from the University of Colorado, as well as standalone IDL programs. All of our analyses utilize products from the CalCOS pipeline. A detailed description of our analyses is presented in the following subsections.

#### **3.3.1 Spatial Resolution Analysis**

To trace the dependence of the spatial profile in the FUV spectra with wavelength, we used the two-dimensional **flt** files generated by CalCOS v2.12a from program 11897. The **flt** files from these observations contain calibrated two-dimensional images of each detector segment, and show the deadtime-corrected count rate at each pixel. (Note that as of CalCOS v2.12a, flat field corrections have not yet been included for FUV data). Using a task-specific IDL code, we summed the **flt** spectra within the active area of each segment in a series of adjacent intervals along dispersion, each 100 pixels wide. This produced ~ 140-150 one-dimensional profiles in the spatial direction for the G130M and G160M data. For analysis of the G140L data we only worked with the Segment A spectra. We did not extract profiles from the entire segment of G140L data because the continuum emission from WD0947+857 fades rapidly at wavelengths longer than 1600 Å. In addition, second order light from the object begins to emerge on the latter 1/3 of Segment A ( $\lambda > 2150$  Å). Therefore, we limited our extractions to the first 2/3 of the detector, obtaining ~ 120 one-dimensional profiles for our G140L analysis.

### **3.3.2 FUV Plate Scale Analysis**

The **corrtag** (corrected time-tag) files were used from our observations of LIN 358 during SMOV (PID 11490) to analyze the data. These files contain calibrated two-dimensional images of each detector segment showing total integrated counts versus pixel position. For each detector, we selected a bright, isolated line. We created one-dimensional profiles in both the dispersion and cross-dispersion directions. In the dispersion direction, we fit the line profile with a Gaussian and recorded the XFULL (the calibrated X pixel values) center position, as well as the Gaussian FWHM and peak value to track how the line strength varied as the star was moved in the aperture. In the cross-dispersion direction, the profiles are highly variable and show non-Gaussian wings from the MFWFEs. However, the profiles have strong enough central peaks to allow an approximate characterization via Gaussian fits. We used a Gaussian fit to define the YFULL (the calibrated Y pixel values) center position of the profile and then directly measured the FWHM of the profiles and the counts in the brightest pixel (results are reported in **Tables 3-5**). Due to the very low background of the FUV detector, background subtraction was ignored for this analysis. All plate scale analysis was performed using CEDAR.

### **3.3.3 Aperture Throughput Analysis**

To obtain the change in flux as a function of offset within the COS aperture (i.e., the aperture throughput), we used the LIN 358 spectra from program 11490. We utilized one-dimensional **x1d** spectra from the data at each POSTARG position using CalCOS v2.12a. Since the POSTARG shifts move the object spectrum to different pixels in cross-dispersion (Y), the PSA – WCA separation changes between each exposure. Therefore, we specified separate spectral extraction parameters for each CalCOS run, shifting the Y centers of both the object and sky extraction boxes by the number of pixels the object spectrum has moved.

## **4. Results**

The results from our spatial analysis of SMOV data and Cycle 17 calibration data are shown below.

### **4.1 Spatial Resolution Results**

The spatial resolution is often defined via the Rayleigh criterion, i.e., it is the angular separation between two equally bright point sources when the peak from one source falls onto the first minimum in the diffraction pattern (Airy disk) of the other. When this occurs, the peak to peak distance between the two sources is nearly equal to the FWHM

**Table 1.** Filenames of COS exposures used in the spatial resolution analysis.

| Filename<br>(*_flt_(a,b).fits) | Grating | Cenwave<br>(Å) | FPPOS | Aperture | Exposure time<br>(s) | PID   |
|--------------------------------|---------|----------------|-------|----------|----------------------|-------|
| lbb909ppq                      | G130M   | 1291           | 3     | PSA      | 310                  | 11897 |
| lbb909pnq                      | G130M   | 1309           | 3     | PSA      | 365                  | 11897 |
| lbb909psq                      | G130M   | 1327           | 3     | PSA      | 420                  | 11897 |
| lbb919dxq                      | G160M   | 1577           | 3     | PSA      | 330                  | 11897 |
| lbb919e3q                      | G160M   | 1589           | 3     | PSA      | 360                  | 11897 |
| lbb919dzq                      | G160M   | 1600           | 3     | PSA      | 390                  | 11897 |
| lbb919e5q                      | G160M   | 1611           | 3     | PSA      | 420                  | 11897 |
| lbb919e1q                      | G160M   | 1623           | 3     | PSA      | 460                  | 11897 |
| lbb909pfq                      | G140L   | 1105           | 3     | PSA      | 200                  | 11897 |
| lbb909plq                      | G140L   | 1230           | 3     | PSA      | 160                  | 11897 |
| la9t24i7q                      | G130M   | 1291           | 4     | BOA      | 540                  | 11492 |
| la9t24ibq                      | G130M   | 1327           | 1     | BOA      | 540                  | 11492 |
| la9t24imq                      | G160M   | 1577           | 4     | BOA      | 780                  | 11492 |
| la9t24isq                      | G160M   | 1623           | 1     | BOA      | 780                  | 11492 |
| la9t24jfq                      | G140L   | 1105           | 4     | BOA      | 360                  | 11492 |
| la9t24izq                      | G140L   | 1230           | 1     | BOA      | 360                  | 11492 |

of each individual source. Therefore, in our analysis of the white dwarf spectra we characterize the spatial resolution by measuring and quoting the full width half maximum (FWHM) of an unresolved point source profile perpendicular to dispersion.

A cursory examination of the two-dimensional white dwarf spectra from the FUV sensitivity monitoring program shows that the shapes and widths of the spatial profiles vary strongly with wavelength (**Figures 2 – 6**). The spatial profiles are broadest on Segment B of the G130M spectra – the shortest wavelengths covered by the COS medium resolution modes. In addition to being broad, the centers of the G130M spatial profiles are also strongly non-Gaussian, exhibiting double-peaked shapes. On the other hand, the



spatial profiles of the G160M spectra are single-peaked, and are considerably narrower than the G130M profiles. The Segment A spectra with the G140L grating also show single-peaked spatial profiles, with the profiles exhibiting a wider range in widths than either the G130M or G160M spectra. Perhaps most significantly, *the widths of the spatial profiles exhibit a strong dependence on central wavelength (CENWAVE) setting.* For a given grating, the spatial profiles become progressively narrower at progressively longer CENWAVE settings.

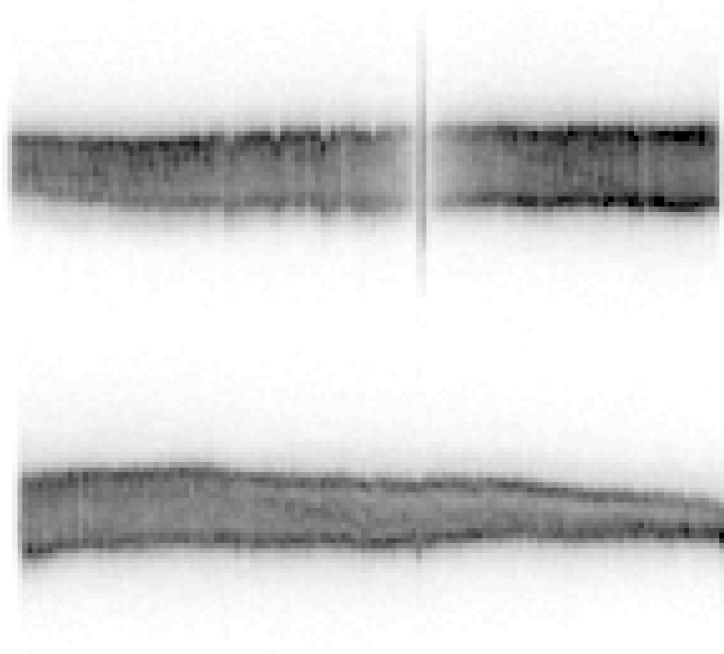


**Figure 2.** Full two-dimensional G130M **corrtag** spectra of WD0947+857 (square root intensity stretch) at central wavelength of 1291 Å, PSA aperture, showing Segment B (top) and Segment A (bottom). The vertical feature in the top spectrum is the Lyman alpha airglow line. Horizontal dimension is wavelength (binned by 100 pixels in XFULL, or 1 Å pixel<sup>-1</sup>) and vertical dimension is cross-dispersion (spatial, corresponding to YFULL). The vertical ripples seen in the spectra are residual geometric distortions not currently corrected by CalCOS. Maximum height of the spectrum perpendicular to dispersion is ~ 19 pixels FWHM for Segment B, ~ 17 pixels for Segment A.

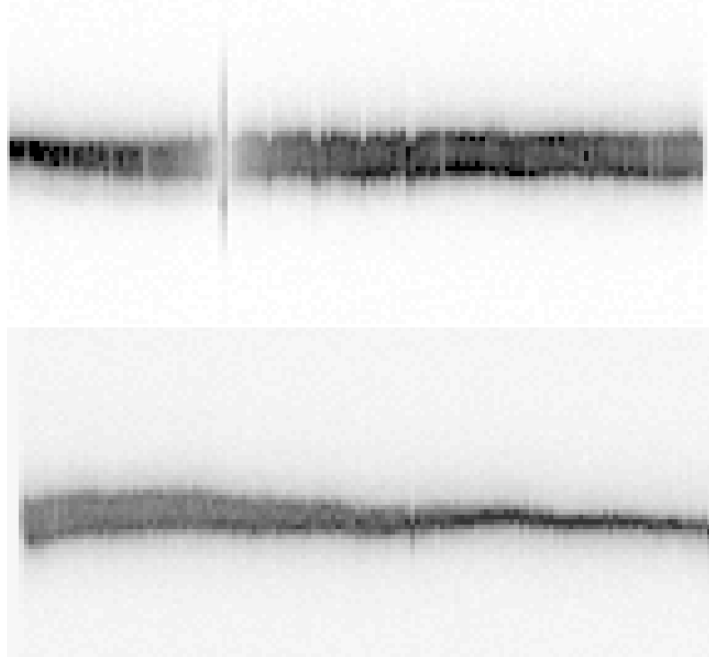


**Figure 3.** Same as **Figure 2**, but for CENWAVE = 1327 Å. The spatial profiles are conspicuously narrower here than at shorter central wavelength settings (compare to **Figure 2**). Maximum height of the spectrum perpendicular to dispersion is ~ 11 pixels FWHM for Segment B, ~ 9 pixels for Segment A.

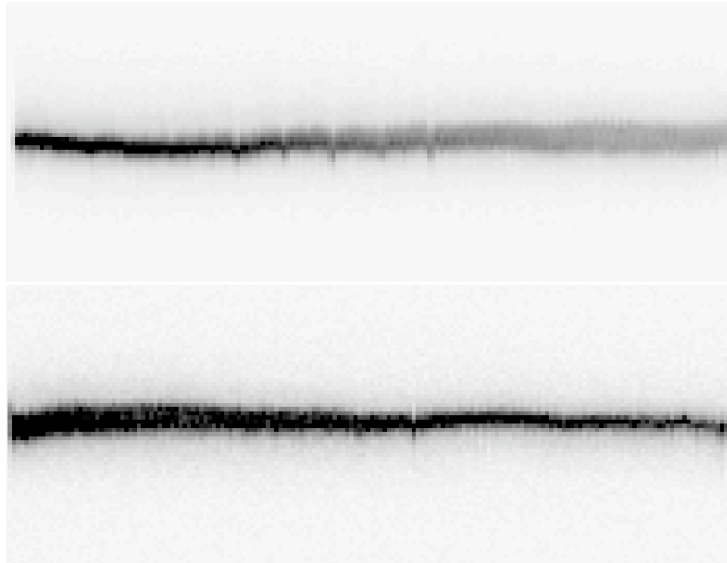


**Figure 4.** Full 160M **corrtag** spectra of WD1057+719 (square root intensity stretch) at central wavelength of 1577 Å, PSA aperture, showing Segment B (top) and Segment A (bottom). Horizontal dimension is wavelength (corresponding to XFULL binned by 100 pixels, or 1 Å pixel<sup>-1</sup>), with the vertical dimension being cross-dispersion (spatial, corresponding to the YFULL dimension). Maximum height of the spectrum is ~ 9 pixels FWHM perpendicular to dispersion for both Segments A and B. The vertical ripples seen in the spectra are residual geometric distortions not currently corrected by CalCOS.

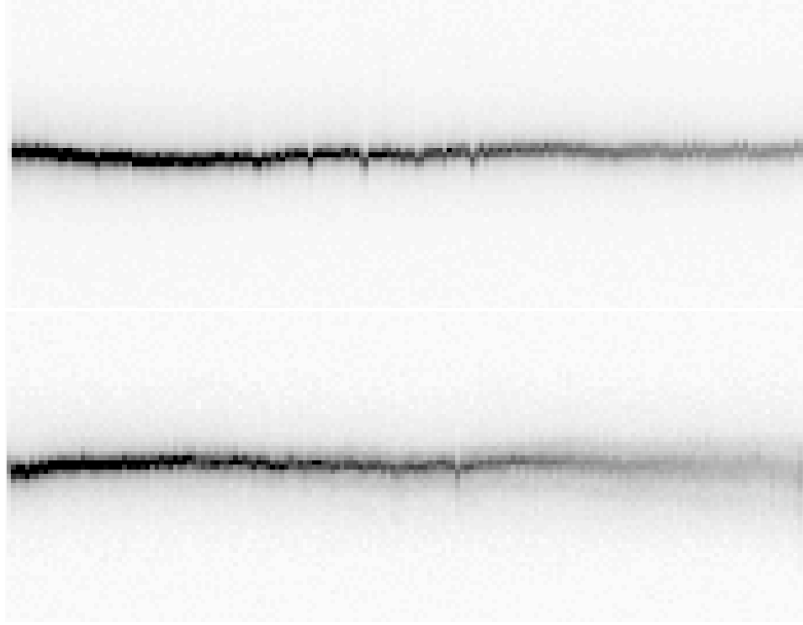


**Figure 5.** Same as **Figure 4**, but for CENWAVE = 1623 Å. Maximum height of the spectrum is ~ 3 pixels FWHM perpendicular to dispersion for Segment B and ~ 5 pixels for Segment A.

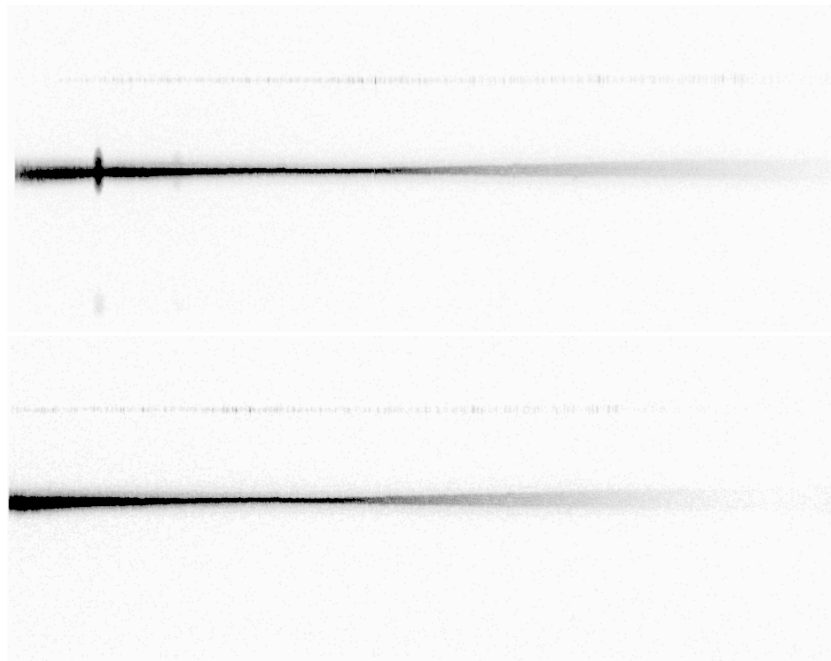


**Figure 6.** G140L **corrtag** spectra of WD0947+857 (square root intensity stretch), PSA aperture, showing the Segment A spectrum at 1105 Å (top) and 1230 Å (bottom). The vertical feature the top spectrum is the Lyman alpha airglow line. Horizontal dimension is wavelength (corresponding to XFULL binned by 13 pixels, or 1 Å pixel<sup>-1</sup>) while the vertical dimension is cross-dispersion (spatial, corresponding to YFULL). The faint spectra seen at the top of each object spectrum is the wavecal spectrum.

The above results are captured in the plots in **Figure 7**, where the FWHM of spatial profiles are shown as a function of wavelength for the FUV gratings. The FWHM was obtained by fitting a Gaussian function with a linear baseline to spatial profiles (obtained as described earlier by collapsing the spectra in the **flt** images every 100 pixels along dispersion). Each 100-pixel sum corresponds to roughly 1 Å for the M gratings, and ~ 8 Å for the L grating. Note that the detailed shapes of the double-peaked spatial profiles are poorly described by a single Gaussian profile in the G130M spectra. However, the fitted Gaussian FWHM is still useful for broadly characterizing how the shapes and widths of the spatial profiles change with both wavelength and CENWAVE setting. We converted the FWHM of the profiles from pixels to arcseconds by multiplying the widths by the cross-dispersion plate scale for each detector, which we assume to be 0.1" pixel<sup>-1</sup> for G130M, 0.09" pixel<sup>-1</sup> for G160M and 0.09" pixel<sup>-1</sup> for G140L (derived from our plate scale analysis described in Section 4.2). For each set of 100 pixels summed along dispersion, we used the dispersion relation for that grating and central wavelength setting to compute the wavelength at the central pixel from that set (i.e., pixels 50, 150, 250, ...). We then assigned that wavelength to the FWHM of each of the 100-pixel summed profiles.

The systematic narrowing of the spatial profile with increasing CENWAVE setting can be clearly seen in **Figure 7**. The narrower profile, in turn, indicates better spatial focus and increased spatial resolution with increasing CENWAVE setting (each of the observations is performed at the same FPPOS=3 setting). By contrast, from an examination of data from other programs, we find that for a given FUV grating and CENWAVE setting there is minimal change in the widths of spatial profiles between different FPPOS settings.

The small fluctuations seen in the fitted FWHM of the spatial profiles (**Figure 7**) are dominated not by the statistical noise, which is much smaller than the observed fluctuations, but rather the residual structure on the FUV detectors (e.g., dead spots, grid wires, etc) as well as residual small-scale geometric distortions uncorrected by CalCOS. Some of the fluctuations are also due to the presence of spectral absorption lines.

Additional systematic trends can be seen at each CENWAVE in the profile plots in **Figure 7**. For Segment B spectra from both G130M and G160M, the spatial profiles are narrowest at the shortest wavelengths and become progressively broader at longer wavelengths. The opposite trend is seen for the Segment A G130M spectra, while all the profiles of the Segment A G160M spectra reach a common minimum near 1700 Å, before broadening again at the longest wavelengths. The profiles in the G140L Segment A spectra (we do not consider the G140L Segment B data here) reach a minimum width between 1400 Å and 1550 Å, and progressively broaden out to shorter and longer wavelengths. The results of a 4<sup>th</sup>-order polynomial fit to the spatial profiles as a function of wavelength in **Figure 7** are presented in the Appendix. Observers can use the tabulated polynomial coefficients to gauge the spatial resolution of the COS FUV channel as a function of wavelength for a given grating and CENWAVE setting.

The systematic variations in shapes and widths of the spatial profiles result from the

layout of the COS FUV channel. The aspheric FUV gratings used in COS are shaped to correct for the spherical aberration of HST (both along dispersion and perpendicular to it), while the holographic rulings on the gratings simultaneously disperse the light from the HST OTA and correct for the astigmatism inherent in the modified Rowland circle layout of the FUV channel (the MFWFEs are of course not corrected). However, the holographic solution only minimizes the cross dispersion height at two wavelengths, hence the cross dispersion profile is expected to be significantly larger at other wavelengths. Furthermore, the cross dispersion solution is only optimized at one central wavelength setting, so the minimum height increases away from the optimized geometry. This results in the wide variations in profile FWHM (and hence spatial resolution) seen in **Figure 7**. The changing FWHM with wavelength is similar to what is seen in FUSE spectra, where a Rowland circle layout is employed.

The spatial and spectral focus vary independently in the COS FUV channel: for a given FUV grating, COS is designed to produce spectra having nearly constant spectral resolution with wavelength (corresponding to constant focus along the dispersion). This is accomplished by placing the COS FUV detector along the Rowland circle and approximately matching the curvature of the detector to match that of the Rowland circle. This leaves the spatial (cross-dispersion) focus to vary along the detector. The surface of constant spatial focus intersects the detector at two points, one on Segment A and one on Segment B. By design, these focus points correspond to wavelengths of 1150 Å and 1450 Å for G130M and 1350 Å and 1750 Å for G160M, which is approximately what is observed in **Figure 7**. Elsewhere, the spatial profile is not at optimum focus. This is adequate for the majority of cases where the science targets are isolated point sources, and the flux is merely collapsed along cross-dispersion to produce the final **x1d** spectra. However, in a moderately crowded field (for example, several point sources located ~ 0.5" apart from one another in cross-dispersion), the extent of the spatial profile will require consideration. At a given wavelength, two sources may overlap spatially at one central wavelength setting, but not at another. The overlap between spectra is even more important if one or more of the sources is extended.

The trends described above for data acquired with the PSA are also seen in data taken with the BOA. In **Figures 8-10** we show the same plots as **Figures 2-6**, except for the BOA data. The spectra here (GD71 was observed with all three gratings) were acquired as part of an FUV sensitivity test during SMOV, so the observations were done at the two most extreme FPPOS settings to cover the largest wavelength range possible. As shown in **Figures A4** and **A5** in the Appendix, the spatial profiles of the BOA spectra exhibit broad asymmetric wings extending toward smaller pixels (to the left of the main peak). These wings are the result of coma and are produced by the neutral density filter of the BOA (which are responsible for the chevron-shaped PSF of point sources observed in the NUV imaging data; see Chapter 8 of the Cycle 18 COS Instrument Handbook).

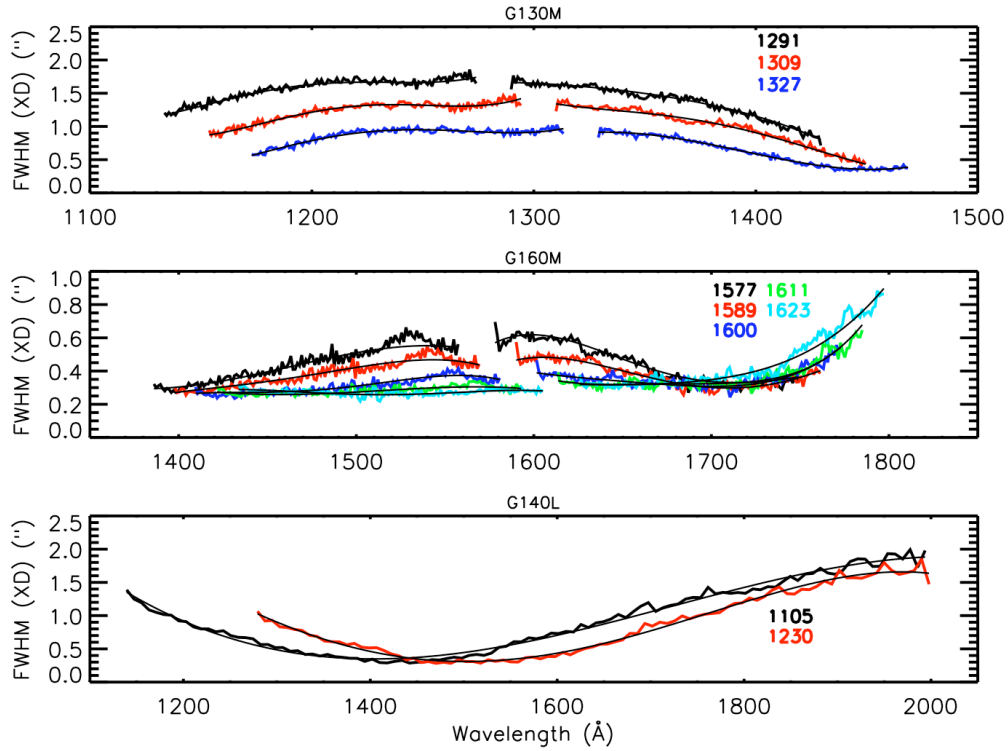


**Figure 7.** Variation of the height of the FUV spatial profile, obtained from the Cycle 17 sensitivity monitoring program data. The widths are obtained via Gaussian fits to the cross-dispersion profiles of the white dwarfs WD0947+857 (G130M and G140L) and WD1057+719 (G160M), observed through the PSA aperture. Widths are plotted as a function of wavelength for each of the central wavelength settings. Airglow features in the G130M and G140L spectra have been interpolated over. The thin black lines drawn through each of the curves indicate polynomial fits to the cross-dispersion (coefficients tabulated in the Appendix).

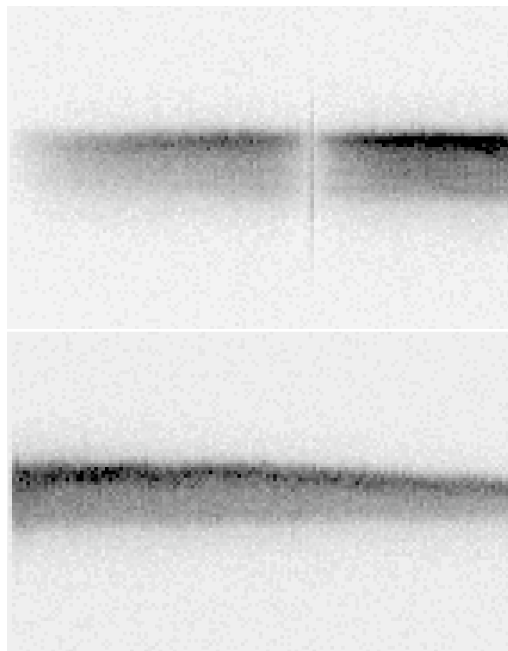


**Figure 8.** G130M **corrtag** spectra of GD 71 (square root intensity stretch), BOA aperture, CENWAVE = 1291, showing the Segment B spectrum (top) and Segment A spectrum (bottom). Horizontal dimension is wavelength (binned by 100 pixels in XFULL, or  $1 \text{ \AA pixel}^{-1}$ ) and vertical dimension is cross-dispersion (spatial, corresponding to YFULL). The vertical feature in the top spectrum is the Lyman alpha airglow line.

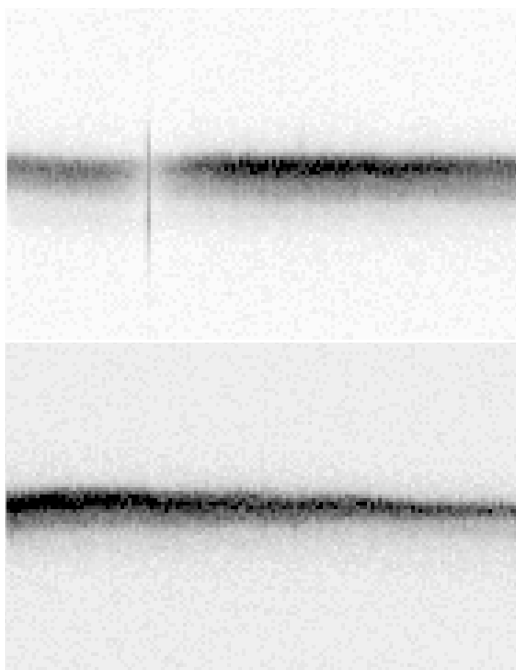


**Figure 9.** Same as **Figure 8**, but at CENWAVE=1327.

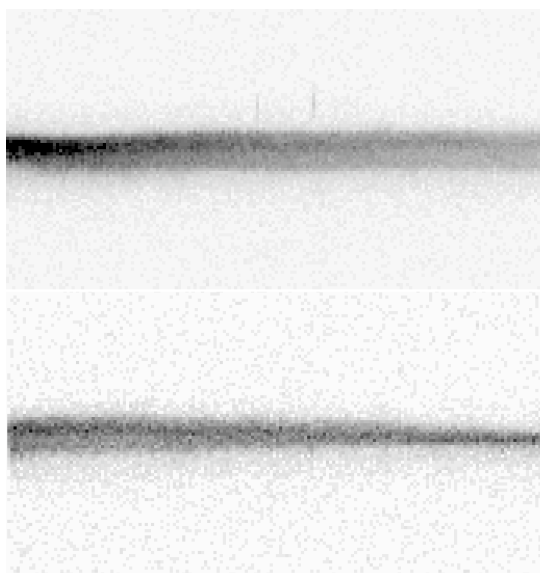


**Figure 10.** Two-dimensional G160M spectra of GD 71 (square root intensity stretch), BOA aperture, CENWAVE=1577, showing the Segment B spectrum (top) and Segment A spectrum (bottom). Horizontal dimension is wavelength (binned by 100 pixels in XFULL, or  $1 \text{ \AA pixel}^{-1}$ ) and vertical dimension is cross-dispersion (spatial, corresponding to YFULL).

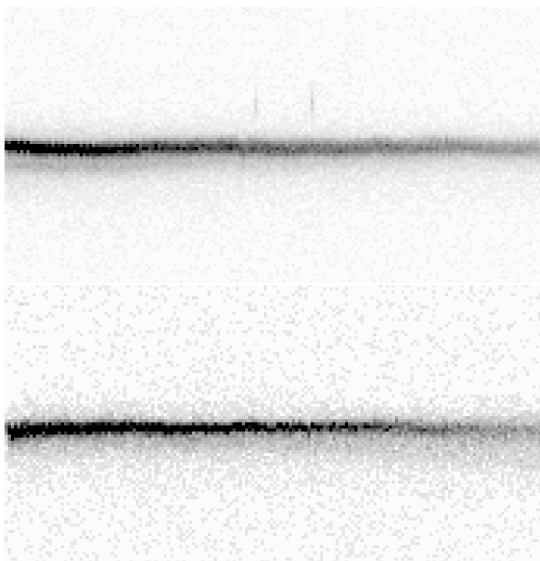


**Figure 11.** Same as Figure 10, but for CENWAVE = 1623.



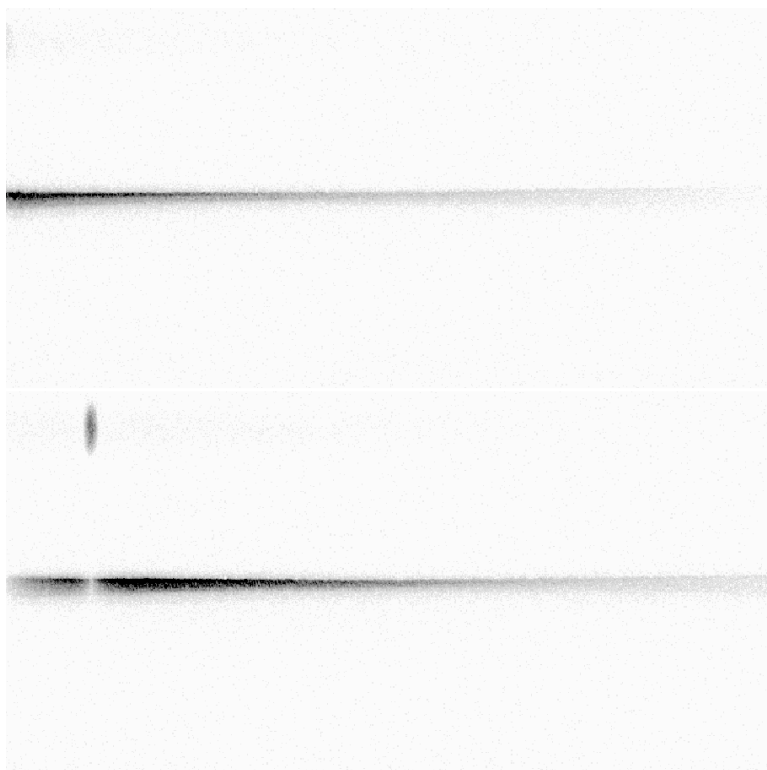


**Figure 12.** Two-dimensional G140L spectra of GD 71 (square root intensity stretch), BOA aperture, showing the Segment A spectrum at 1230 Å (top) and 1105 Å (bottom). The vertical feature seen in the upper left corner of the lower spectrum is Lyman alpha airglow entering through the PSA aperture. Horizontal dimension is wavelength (corresponding to XFULL binned by 13 pixels, or 1 Å pixel<sup>-1</sup>) while the vertical dimension is cross-dispersion (spatial, corresponding to YFULL).

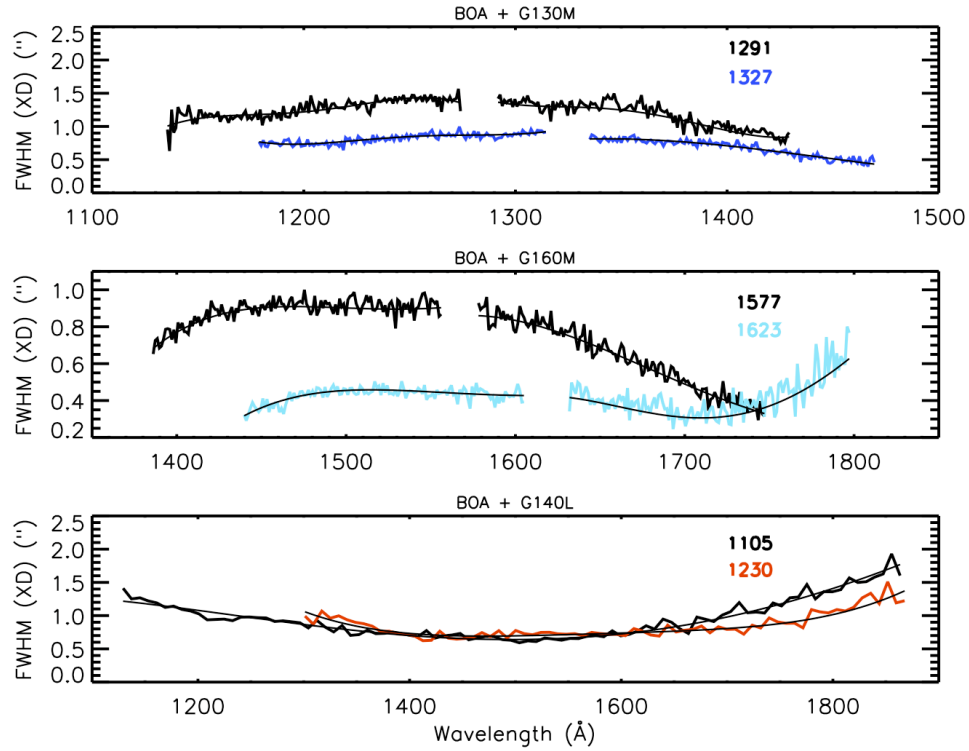


**Figure 13.** Variation of the height of the spatial profile from BOA observations in the SMOV program 11492 (“FUV Sensitivity”). The widths are obtained via Gaussian fits to the cross-dispersion profiles of the white dwarf GD71. Widths are plotted as a function of wavelength for each of the central wavelength settings. Note that the single Gaussian fit slightly underpredicts the height of the profile (by  $\sim 15\%$ ) for G130M, which has an asymmetric profile with a broad wing as shown in **Figures 8, 9** and **A4**. The results in Figure 13 are approximate. Airglow features in the G130M and G140L spectra have been interpolated over. The thin black lines drawn through each of the curves indicate the polynomial fits to the cross-dispersion width as a function of wavelength (coefficients are tabulated in the Appendix).

#### 4.2 FUV Plate Scale Results

We can utilize the shifts computed from the spectra to calculate the plate scale of the COS FUV detector for the three gratings. Since the offsets are specified in arcseconds (POSTARG) and the shifts are recorded in pixels, we can obtain the plate scale by dividing the two quantities. Each POSTARG gives a separate measurement of the plate scale, as well as a measure of the dependence of the shifts between dispersion and cross-dispersion.

The relationship between dispersion and cross-dispersion shifts can be characterized via the following pair of equations (a similar definition is used for the NUV; see Bèland & Ghavamian 2010):

$$\begin{aligned}
\Delta Y_{\text{pix}} &= \alpha_{YY} \Delta Y''_{\text{POSTARG}} + \alpha_{YX} \Delta X''_{\text{POSTARG}} \\
\Delta X_{\text{pix}} &= \alpha_{XY} \Delta Y''_{\text{POSTARG}} + \alpha_{XX} \Delta X''_{\text{POSTARG}}
\end{aligned}
\tag{1}$$

Where  $\Delta X''$  and  $\Delta Y''$  are the specified POSTARG shifts along dispersion and along cross-dispersion in arcseconds, and  $\Delta X_{\text{pix}}$  and  $\Delta Y_{\text{pix}}$  are the resulting shifts on the NUV detector in pixels. The  $\alpha$  factors are the plate scale coefficients in units of pixels/arcsecond. The subscripts on the coefficients can be interpreted in the following way:  $\alpha_{XY}$  is the pixel shift along dispersion (X) produced by a specified POSTARG of 1" perpendicular to dispersion (Y), and so on. The coefficients  $\alpha_{XX}$  and  $\alpha_{YY}$  are the plate scales along dispersion and perpendicular to dispersion, respectively. For a given emission line, we estimated the  $\alpha$  coefficients for each exposure, in both the positive and negative directions (i.e., each POSTARG). We then calculated the mean and standard deviation of the coefficients separately for the set of positive and negative POSTARGs. Finally, we computed the average of the two means, weighted by their standard deviations. The resulting values for each grating is shown in **Table 2**. *We find that POSTARGs specified purely along one axis result in negligible shifts in the other dimension ( $\leq 0.5$  pixels), so the cross terms  $\alpha_{XY}$  and  $\alpha_{YX}$  are effectively zero.* The derived coefficients are similar to what was measured in simulations with the Target Acquisition Analysis for COS (TAACOS) program (COS-11-0016, Table 3). For comparison, the OP-01 values for the coefficients are  $\alpha_{XX} = 44.2$  pixels per arcsecond and  $\alpha_{YY} = 10.6$  pixels/arcsecond (assuming the OPO-01 values of 265  $\mu\text{m}$  per arcsecond and 6x25  $\mu\text{m}$  pixels).

Inverting the coefficients, we obtain the plate scales in the more commonly quoted units of arcseconds per pixel: 0.1", 0.09" and 0.09" per pixel in cross-dispersion for G130M, G160M and G140L, respectively, and 0.024 arcseconds per pixel along dispersion for G160M. Since there was no POSTARG sequence along dispersion for G130M and G140L, calculation of the  $\alpha_{XX}$  coefficients for those gratings will be deferred until suitable data become available.

**Table 2.** Plate scale coefficients derived for the COS FUV detector (X is along dispersion, Y is along cross-dispersion). These can be used with Equation (1) to predict the spectral shift for positions offset from the center of the PSA aperture.

| Plate scale<br>(pixels / ") | G130M | G160M | G140L |
|-----------------------------|-------|-------|-------|
| $\alpha_{YY}$               | 9.72  | 11.33 | 10.97 |
| $\alpha_{XX}$               | ...   | 41.13 | ...   |

### 4.3 Aperture Throughput Results

As the target is stepped away in position from the center of the aperture, its flux progressively drops relative to the value measured at the on-center position. This reflects the increasing vignetting of the flux by the edge of the PSA aperture at increasing off-axis positions.

To measure the variation of aperture throughput with off-axis position, we used the **x1d** spectra extracted from each offset spectrum of LIN 358 by CalCOS. For each segment, we obtained the net (background-subtracted) count rates integrated over its the bandpass. Normalizing the fluxes of the off-center positions to that of the on-center position, we produced the PSA aperture throughput curves for the FUV channel shown in **Figures 14-16**.

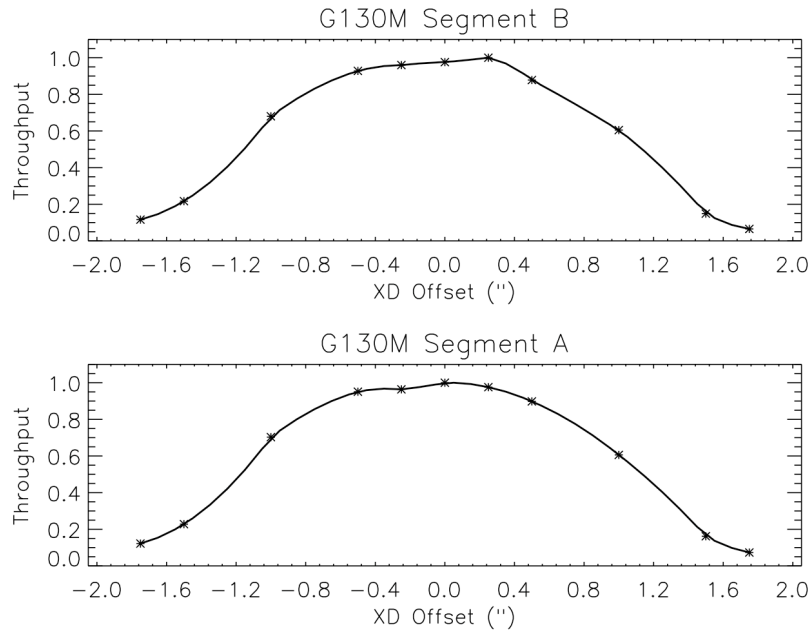


**Figure 14.** The aperture throughput of the FUV channel (G130M grating + PSA aperture). The throughput is nearly constant within  $\pm 0.4''$  from the center of the aperture. The points show the measured values, while the solid curves show a cubic spline fitted through the data.

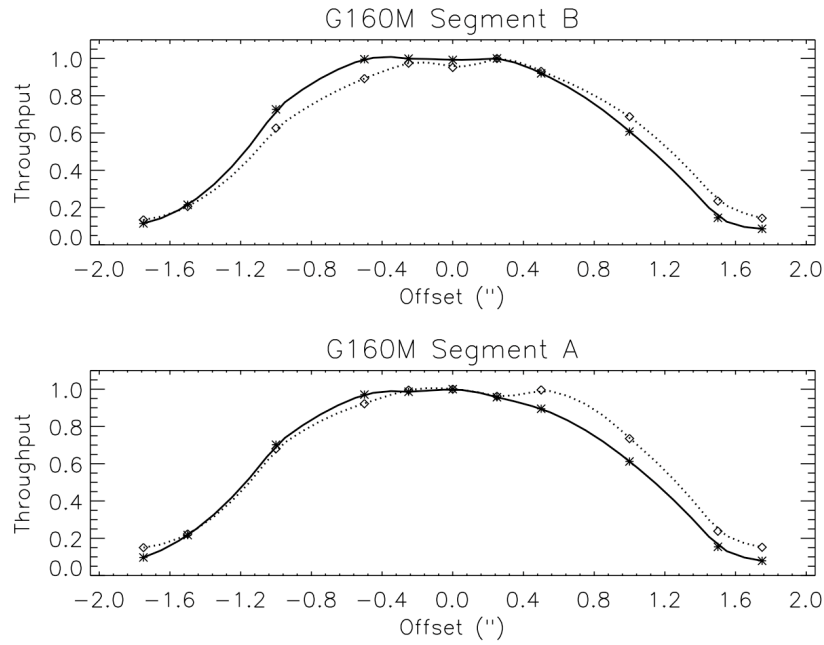


**Figure 15.** The aperture throughput of the FUV channel (G160M grating + PSA aperture) shown for both the dispersion (dotted lines) and cross-dispersion (solid lines) directions. The throughput is nearly constant within  $\pm 0.4''$  from the center of the aperture. The points show the measured values, while the curves show a cubic spline fitted through the data.

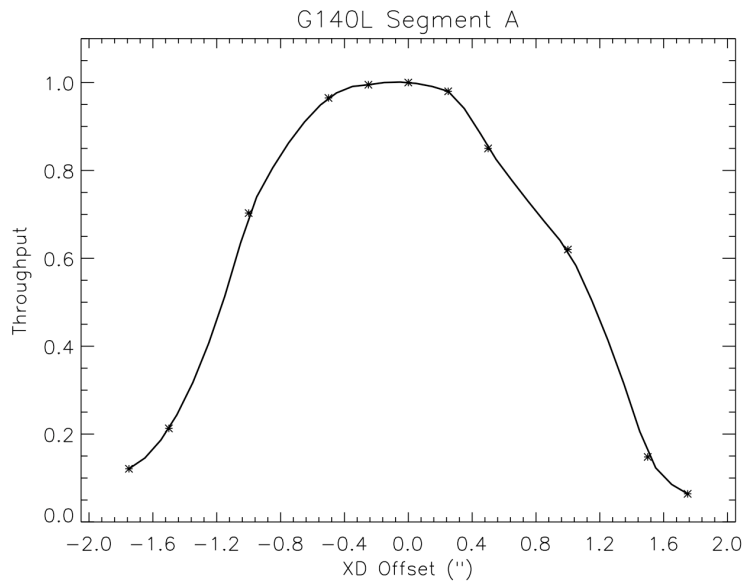


**Figure 16.** The aperture throughput of the FUV channel (G140L grating + PSA aperture) shown in the cross-dispersion direction. The points show the measured values, while the solid curves show a cubic spline fitted through the data.

The maximum in the G130M throughput curve for Segment B occurs near an offset of +0.25" in cross-dispersion (**Figure 14**). However, this asymmetry is unlikely to be real because a corresponding offset in the maximum of the throughput curve does not occur for Segment A of G130M. The G160M aperture throughput curve appears symmetric in cross-dispersion (solid lines in **Figure 15**), as does the curve for G140L (**Figure 16**). However, the G160M curves for both Segments A and B show a significant offset toward positive shifts along dispersion (dotted line in **Figure 15**). The size of the shift is  $\sim 0.25''$ , and may indicate that the target was slightly offset along dispersion from the center of the aperture in the G160M observations.

Note that since the target used for creating aperture throughput curves (LIN 358) is a point source with an emission line spectrum, the throughput values shown in **Figures 14-16** are dominated by count rates recorded at localized points on the detector. This makes the measured fluxes more susceptible to fixed pattern noise as the source is displaced from the center of the aperture (a description of the fixed patterns on the FUV detector is presented in Section 6.8.1 of the COS Cycle 18 Instrument Handbook). On the other hand, the orbit-to-orbit repeatability for each grating setup, as measured by the standard deviation in net count rates between the four G160M exposures at POSTARG=(0,0), is  $\sim 3\%$  and  $1\%$  for Segments A and B, respectively. Adopting the larger number as the more conservative estimate of the repeatability for all the gratings ( $3\%$ ), we conclude that with the errors on the flux measurements (due to a combination of statistical errors, fixed pattern noise and repeatability) the aperture throughput curves in **Figures 14-16** are consistent with a symmetric shape, at least until higher signal-to-noise data become available and provide convincing evidence to the contrary.

#### ***4.4 Off-Axis Variation of the FUV Spatial Profile***

As the target (LIN 358) is stepped toward the edge of the PSA aperture, the vignetting of the source produces variations in both flux and shape of the FUV line profiles. Here we present spatial profile plots for the G130M, G160M and G140L spectra at each of the POSTARG positions in cross-dispersion. For G130M we used the N V  $\lambda 1238$  emission line located on the B segment and the Si IV  $\lambda 1393$  line located on the A segment to examine variations in the shape of the cross-dispersion profile with position away from the aperture center. For G160M and G140L we plotted the He II  $\lambda 1640$  profile on Segment A.

**Table 3** gives the measured parameters for the N V line profile and strength for the different spectra and aperture positions. In **Figure 17** we plot the spatial profile of the N V  $\lambda 1238$  Å emission line as the star is shifted perpendicular to dispersion. At small distances from the center of the aperture ( $0.25''$ ), the cross-dispersion profile exhibits the double-peaked shape characteristic of the astigmatism at the shortest CENWAVE settings of G130M (as seen in **Figures 2** and **A1**). At offsets exceeding  $0.5''$ , the cross-dispersion profiles become increasingly asymmetric as one side of the double-peaked profile becomes increasingly vignettted by the edge of the PSA aperture. This has the effect of narrowing the cross-dispersion profile, as seen in **Figure 2** and reflected by the reduction

in YFWHM reported in **Table 3**. The values of YFWHM for the N V  $\lambda 1238$  Å line are consistent with values reported **Figure 7** at 1238 Å.

**Table 3.** Fitted positions, peak counts, and profile widths in the cross-dispersion and dispersion directions for the N V  $\lambda 1238$  Å emission line in the G130M spectra of LIN358 (PID 11490). The Y values are measured directly from the observed cross-dispersion profile while the X values are the Gaussian fit parameters to the spectral profile of the line.

| Filename<br>(*_corrtag_b.fits) | POSTARG<br>(X,Y)("") | Ycenter<br>(pix) | Ypeak<br>(cnts) | YFWHM<br>(pix) | Xcenter<br>(pix) | Xpeak<br>(cnts) | XFWHM<br>(pix) |
|--------------------------------|----------------------|------------------|-----------------|----------------|------------------|-----------------|----------------|
| labn01e3q                      | (0,0)                | 545.0            | 526             | 12.6           | 10033.4          | 174.9           | 33.0           |
| labn01e5q                      | (0,0.25)             | 548.8            | 599             | 12.0           | 10033.0          | 168.3           | 33.5           |
| labn01e7q                      | (0,0.50)             | 551.0            | 543             | 12.0           | 10033.0          | 168.3           | 32.7           |
| labn01e9q                      | (0,1.0)              | 555.3            | 501             | 7.0            | 10033.0          | 109.3           | 35.1           |
| labn01eeq                      | (0,1.5)              | 558.8            | 201             | 2.9            | 10033.5          | 27.0            | 34.4           |
| labn01egq                      | (0,1.75)             | 561.1            | 71              | 2.9            | 10032.8          | 11.8            | 34.6           |
| labn01eiq                      | (0,0)                | 545.5            | 526             | 13.1           | 10033.6          | 174.8           | 33.9           |
| labn01ekq                      | (0,-0.25)            | 542.5            | 545             | 13.0           | 10033.6          | 180.4           | 34.1           |
| labn01emq                      | (0,-0.50)            | 539.3            | 547             | 12.0           | 10033.3          | 177.7           | 33.4           |
| labn01eoq                      | (0,-1.0)             | 535.1            | 551             | 6.0            | 10033.2          | 130.7           | 33.0           |
| labn01eqq                      | (0,-1.5)             | 532.5            | 291             | 3.3            | 10033.2          | 41.3            | 33.2           |
| labn01esq                      | (0,-1.75)            | 529.8            | 181             | 3.0            | 10033.1          | 32.5            | 32.1           |

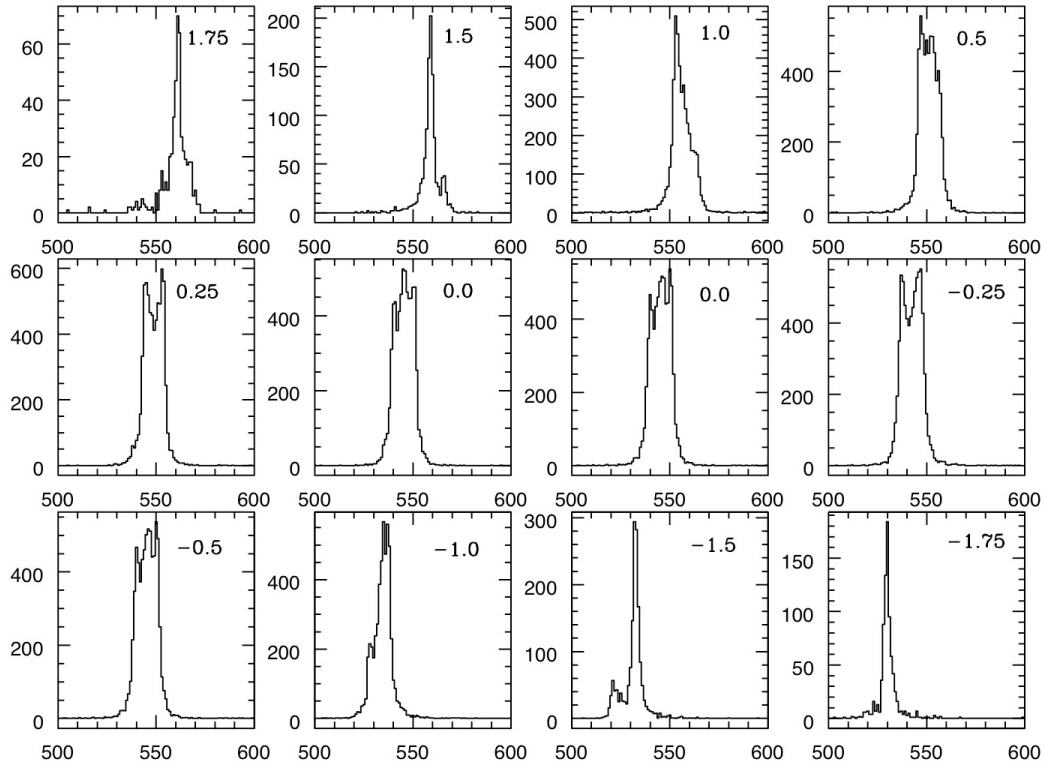


**Figure 17.** Cross-dispersion profiles for G130M, Segment B, shown for various offsets in cross-dispersion (Y, labeled in the upper right of each panel in arcseconds). Each frame shows the cross-dispersion profile for the N V  $\lambda 1238$  emission line in LIN 358. Note the double-peaked shape of the profile at  $\pm 0.25''$  (reflecting the astigmatism from the G130M grating) and the vignetting of one side of the profile as the source is moved close to the edge of the PSA aperture.

In **Table 4** we present the measured parameters for the He II at the different aperture positions. The observations in G160M stepped the star in both the cross-dispersion (Y) and dispersion (X) directions in the PSA. **Figure 18** shows the spatial profiles of the He II line as the star is stepped through the PSA perpendicular to dispersion. The profiles are considerably narrower than those observed in the G130M spectrum, consistent with the plotted curves in **Figure 7**. The spatial profile for G140L is shown in **Figure 19**. The YFWHM values for the He II line in the G160M and G140L spectra are both consistent with the values shown in **Figure 7**.



**Table 4.** Fitted positions, peak counts, and profile widths in the cross-dispersion and dispersion directions for the He II  $\lambda 1640$  emission line in the G160M spectra of LIN358 (PID 11490).

| Filename<br>(*_corrtag_a.fits) | POSTARG<br>(X,Y)("") | Ycenter<br>(pix) | Ypeak<br>(cnts) | YFWHM<br>(pix) | Xcenter<br>(pix) | Xpeak<br>(cnts) | XFWHM<br>(pix) |
|--------------------------------|----------------------|------------------|-----------------|----------------|------------------|-----------------|----------------|
| labn01euq                      | (0,0)                | 482.8            | 222             | 5.1            | 5441.8           | 32.3            | 37.5           |
| labn01ewq                      | (0,0.25)             | 485.7            | 208             | 6.7            | 5440.7           | 29.3            | 41.5           |
| labn01eyq                      | (0,0.50)             | 488.8            | 193             | 5.0            | 5441.1           | 28.2            | 38.7           |
| labn01f0q                      | (0,1.0)              | 493.9            | 177             | 3.0            | 5442.3           | 18.8            | 39.0           |
| labn01f2q                      | (0,1.5)              | 497.6            | 44              | 3.8            | 5441.1           | 4.8             | 33.2           |
| labn01f4q                      | (0,1.75)             | 500.1            | 18              | 5.7            | 5438.4           | 2.4             | 42.2           |
| labn01f6q                      | (0,0)                | 482.8            | 208             | 5.2            | 5439.8           | 30.7            | 40.4           |
| labn01f8q                      | (0,-0.25)            | 480.1            | 228             | 6.0            | 5441.2           | 31.3            | 38.2           |
| labn01faq                      | (0,-0.50)            | 477.3            | 219             | 5.9            | 5440.6           | 28.9            | 41.3           |
| labn01fcq                      | (0,-1.0)             | 471.2            | 148             | 6.0            | 5440.3           | 22.1            | 41.6           |
| labn01feq                      | (0,-1.5)             | 466.2            | 73              | 2.1            | 5437.6           | 6.4             | 43.3           |
| labn01fgq                      | (0,-1.75)            | 463.3            | 36              | 3.1            | 5439.3           | 3.1             | 43.1           |
| lanb01fiq                      | (0,0)                | 482.9            | 225             | 4.8            | 5439.6           | 30.5            | 39.7           |
| lanb01fkq                      | (0.25,0)             | 483.2            | 224             | 6.0            | 5452.1           | 31.7            | 38.9           |
| lanb01fmq                      | (0.50,0)             | 483.1            | 198             | 7.0            | 5463.7           | 34.5            | 35.5           |
| lanb01foq                      | (1.0,0)              | 483.0            | 170             | 4.8            | 5484.8           | 23.9            | 38.3           |
| lanb01fqq                      | (1.5,0)              | 482.0            | 59              | 4.0            | 5502.5           | 7.2             | 37.5           |
| lanb01fsq                      | (1.75,0)             | 482.2            | 37              | 4.1            | 5509.2           | 3.4             | 49.1           |
| lanb01fuq                      | (0,0)                | 482.8            | 219             | 6.3            | 5441.2           | 32.9            | 38.6           |
| lanb01fwq                      | (-0.25,0)            | 483.0            | 236             | 5.1            | 5431.2           | 34.3            | 37.2           |
| lanb01fyq                      | (-0.50,0)            | 482.8            | 231             | 5.1            | 5420.7           | 32.3            | 37.0           |
| lanb01g0q                      | (-1.0,0)             | 483.2            | 147             | 6.1            | 5399.0           | 21.4            | 39.4           |
| lanb01g2q                      | (-1.5,0)             | 482.8            | 50              | 5.0            | 5382.4           | 6.2             | 36.1           |
| lanb01g7q                      | (-1.75,0)            | 483.1            | 31              | 3.0            | 5367             | 7.0             | N/A            |

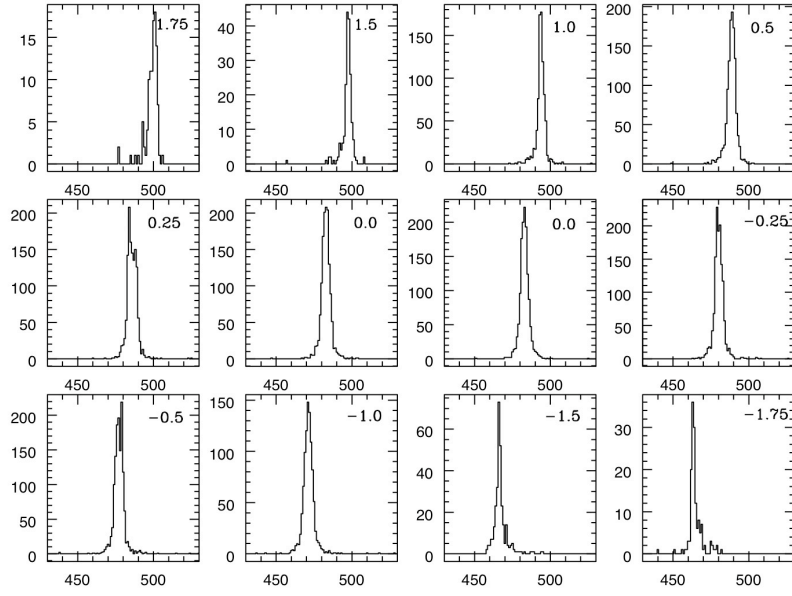


**Figure 18.** Cross-dispersion (spatial) profiles for G160M, Segment A, for various offsets in cross-dispersion (Y, labeled in units of arcseconds in the upper right of each panel). Each frame shows the spectral line profile for the He II  $\lambda 1640$  emission line in LIN 358. The profile narrows at offsets far off-axis ( $\geq 1''$ ), where vignetting by the edge of the PSA aperture becomes important.

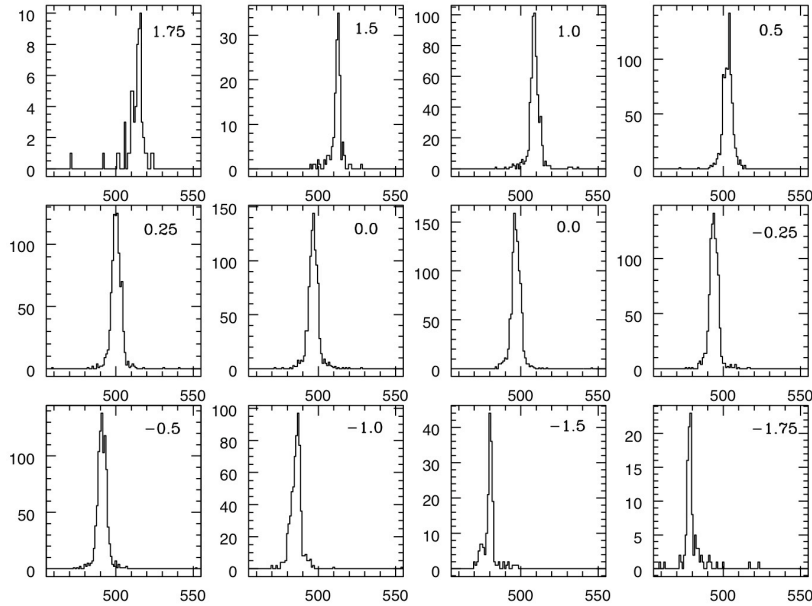


**Figure 19.** Cross-dispersion profiles for G140L, Segment A. Each frame shows the cross-dispersion profile for the He II  $\lambda 1640$  emission line in LIN 358, for different cross-dispersion offsets from the center of the aperture (labeled in the upper right of each panel, in arcseconds).

The profile narrows at offsets far off-axis ( $\geq 1''$ ), where vignetting of the PSF by the edge of the PSA aperture becomes important. For G140L, we again used the He II  $\lambda 1640$  emission line, which is the brightest line in the FUV spectrum of LIN 358. All the data in G140L are located on the A segment of the FUV detector; the B segment, though active, showed no detection of the target due to the greatly reduced effective area at wavelengths  $< 1100 \text{ \AA}$ . **Table 5** gives the measured parameters for the He II line profile and strength for the different spectra and aperture positions.

**Table 5.** Fitted positions, peak counts, and profile widths in the cross-dispersion and dispersion directions for the He II  $\lambda 1640$  emission line in the G140L spectra of LIN358 (PID 11490). Because the dispersion profiles varied from Gaussian, the Xpeak counts give the counts in the strongest pixel rather than the peak of the Gaussian fit.

| Filename<br>(*_corrtag_a.fits) | POSTARG<br>(X,Y)('') | Ycenter<br>(pix) | Ypeak<br>(cnts) | YFWHM<br>(pix) | Xcenter<br>(pix) | Xpeak<br>(cnts) | XFWHM<br>(pix) |
|--------------------------------|----------------------|------------------|-----------------|----------------|------------------|-----------------|----------------|
| labn01g9q                      | (0,0)                | 497.0            | 159.0           | 6.0            | 5913.2           | 84.0            | 10.7           |
| labn01gbq                      | (0,0.25)             | 500.28           | 125.0           | 7.1            | 5912.3           | 74.0            | 10.0           |
| labn01giq                      | (0,0.50)             | 503.0            | 142.0           | 5.8            | 5912.6           | 83.0            | 8.1            |
| labn01gkq                      | (0,1.0)              | 508.8            | 101.0           | 3.9            | 5913.3           | 47.0            | 11.7           |
| labn01gmq                      | (0,1.5)              | 512.6            | 35.0            | 3.0            | 5912.3           | 15.0            | 9.9            |
| labn01goq                      | (0,1.75)             | 514.5            | 10.0            | 3.0            | 5914             | 6.0             | N/A            |
| labn01gqq                      | (0,0)                | 496.8            | 144.0           | 6.9            | 5913.5           | 74.0            | 11.2           |
| labn01gsq                      | (0,-0.25)            | 494.0            | 141.0           | 6.0            | 5913.4           | 75.0            | 11.2           |
| labn01guq                      | (0,-0.50)            | 491.2            | 138.0           | 5.8            | 5913.6           | 66.0            | 12.2           |
| labn01gwq                      | (0,-1.0)             | 486.0            | 97.0            | 5.0            | 5913.4           | 46.0            | 12.3           |
| labn01gyq                      | (0,-1.5)             | 480.3            | 44.0            | 2.2            | 5912.7           | 19.0            | 9.2            |
| labn01hpq                      | (0,-1.75)            | 478.3            | 23.0            | 3.0            | 5910.2           | 11.0            | 10.8           |

## 5. Summary

Analysis of FUV spectra obtained for Parts I and II of “FUV External Spectroscopic Performance” during SMOV have shown that the on-orbit spectral resolution of that channel is significantly impacted by the presence of broad wings on the LSF, a result described in detail by Ghavamian et al. (2009). Although the resolving power of COS remains high ( $R \sim 16,000$ -20,000), the presence of the broad wings requires careful consideration when designing observing programs with the instrument. The spatial resolution of the COS FUV channel along cross-dispersion meets the requirements of the Contract End Item (CEI) specification, with the lowest spatial resolution for the M-mode gratings reached for Segment B of G130M and the highest resolution reached for G160M. However, the spatial resolution for each M-mode grating shows a strong dependence on central wavelength setting used, with the shortest CENWAVEs giving the broadest cross-dispersion profiles (i.e., lowest spatial resolution) and longest CENWAVEs giving the narrowest cross-dispersion profiles (highest spatial resolution). The range for each grating is 0.5" -1.8" for G130M and 0.3"-0.6" for G160M. The corresponding range in spatial resolution for the G140L grating is 0.4"-2.0". For the BOA aperture the values obtained from our analysis are 0.5" -1.5" for G130M, 0.4"-0.9" for G160M and 0.7"-1.5" for G140L, with the G130M values likely being slightly larger than quoted (by  $\sim 15\%$ ) due to our use of a single Gaussian when fitting the asymmetric BOA cross-dispersion profile. The measured spectral resolutions for the PSA and the BOA meet the CEI specification. The spatial resolution, plate scale and aperture throughput of the FUV channel also satisfy the CEI requirements.

## 6. Change History for COS ISR 2010-09

Version 1: 30 September 2010 - Original Document

### References

- Béland, S. & Ghavamian, P., COS Instrument Science Report 2010-08
- COS IDT, “TAACOS: Phase I NUV Report” (COS-11-0016) (2002)
- COS IDT, “Cosmic Origins Spectrograph (COS) Science Operations Requirements Document (OP-01),” (2003)
- COS IDT, “Hubble Space Telescope Cosmic Origins Spectrograph Contract End Item (CEI) Specification” (STE-63) (2004)
- COS IDT, “COS Pre-Launch Calibration Data” Document (AV-04),” (2008)
- Dixon, W. V. et al. 2010, “The Cosmic Origins Spectrograph Instrument Handbook for Cycle 18”, (Baltimore: STScI)
- Ghavamian, P., et al. (2009) COS Instrument Science Report 2009-01(v1)

- Osten, R. et al. (2010) COS Instrument Science report 2010-15
- Vogel, M. & Nussbaumer, H. 1995, A&A, 301, 17

## Appendix

Here we present further results from our analysis of the cross-dispersion profiles for COS FUV spectra. We fit each of the curves shown in **Figures 7** and **13** with a polynomial function in wavelength versus FWHM of the cross-dispersion profile. In the fitting we utilized the error estimates on the FWHM output by the Gaussian fits. The fitted polynomial coefficients are summarized in **Tables A1** and **A2** below, where results are shown for both PSA and BOA spatial profiles. These polynomials can be used to calculate the approximate width of the spatial profile of a point source as a function of wavelength observed in the FUV with COS. The primary contributor to the width variations is the uncorrected astigmatism of the spectrum perpendicular to dispersion.

**Table A1.** Fitted polynomial coefficients for the cross-dispersion width versus wavelength curves (for the PSA aperture) shown in **Figure 7**. The polynomials for each CENWAVE setting are of the form:  $\text{FWHM}_\lambda(\text{''}) = a_0 + a_1*\lambda + a_2*\lambda^2 + \dots a_N*\lambda^N$ , where N is the order of the polynomial (4<sup>th</sup> order for G130M and G160M and G140L). The data used in each fit were acquired at the default FPPOS (=3) setting. The wavelength range covered by each of the fits is indicated below in the far left column, below the CENWAVE listing.

| G130M Seg B                     | A0          | A1       | A2         | A3           | A4           |
|---------------------------------|-------------|----------|------------|--------------|--------------|
| CENWAVE = 1291<br>(1134 – 1274) | 15476.20    | -52.0454 | 00655502   | -3.66455E-05 | 7.67312E-09  |
| CENWAVE = 1309<br>(1154 – 1295) | 23316.90    | -76.9809 | 0.0952103  | -5.22829E-05 | 1.07559E-08  |
| CENWAVE = 1327<br>(1173 – 1313) | 13196.80    | -43.3774 | 0.0533795  | -2.91474E-05 | 5.95926E-09  |
| G130M Segment A                 | A0          | A1       | A2         | A3           | A4           |
| CENWAVE = 1291<br>(1290 – 1430) | -3430.62    | 10.3244  | -0.0116686 | 5.87431E-06  | -1.11177E-09 |
| CENWAVE = 1309<br>(1310 – 1450) | 17235.00    | -50.0389 | 0.0544385  | -2.62974E-05 | 4.75867E-09  |
| CENWAVE = 1327<br>(1329 – 1469) | 2.35221E-07 | -1.25048 | 0.0027077  | -1.94976E-06 | 4.67063E-10  |

**Table A1.** (cont'd)

| G160M Segment B | A0       | A1       | A2         | A3          | A4           |
|-----------------|----------|----------|------------|-------------|--------------|
| CENWAVE = 1577  | -4.74384 | 0.280237 | -0.0005651 | 3.85231E-07 | -8.76513E-11 |

|                                 |          |         |              |             |              |
|---------------------------------|----------|---------|--------------|-------------|--------------|
| (1386 - 1558)                   |          |         |              |             |              |
| CENWAVE = 1589<br>(1398 - 1570) | -3800.30 | 10.4852 | -0.0108443   | 4.98262E-06 | -8.58021E-10 |
| CENWAVE = 1600<br>(1410 - 1580) | -6104.11 | 16.5731 | -0.0168621   | 7.61954E-06 | -1.29019E-09 |
| CENWAVE = 1611<br>(1422 - 1593) | -258.143 | 0.84163 | -9.92243E-04 | 5.06832E-07 | -9.52173E-11 |
| CENWAVE = 1623<br>(1434 - 1605) | -3765.25 | 9.9797  | -0.0099091   | 4.36899E-06 | -7.21700E-10 |

|                                 |           |          |            |              |              |
|---------------------------------|-----------|----------|------------|--------------|--------------|
| G160M Segment A                 | A0        | A1       | A2         | A3           | A4           |
| CENWAVE = 1577<br>(1578 - 1750) | -19053.80 | 45.0421  | -0.0398870 | 1.56829E-05  | -2.31010E-09 |
| CENWAVE = 1589<br>(1590 - 1762) | -10357.30 | 24.1323  | -0.0210463 | 8.14264E-06  | -1.17912E-09 |
| CENWAVE = 1600<br>(1602 - 1773) | -6104.11  | 16.5731  | -0.0168621 | 7.61954E-06  | -1.29019E-09 |
| CENWAVE = 1611<br>(1614 - 1785) | 19213.00  | -45.9071 | 0.0411321  | -1.63787E-05 | 2.44563E-09  |
| CENWAVE = 1623<br>(1626 - 1797) | 4890.68   | -11.915  | 0.0108866  | -4.42489E-06 | 6.74861E-10  |

|                                 |          |           |             |              |              |
|---------------------------------|----------|-----------|-------------|--------------|--------------|
| G140L Segment A                 | A0       | A1        | A2          | A3           | A4           |
| CENWAVE = 1105<br>(1139 - 2000) | 47.8265  | -0.010392 | 4.01432E-05 | -2.47197E-09 | -1.54125E-12 |
| CENWAVE = 1230<br>(1279 - 2000) | -53.9819 | 0.201794  | -2.4464E-04 | 1.2150E-07   | -2.13401E-11 |

**Table A2.** Fitted polynomial coefficients for the cross-dispersion width versus wavelength curves (for the BOA aperture) shown in **Figure 13**. The polynomials for each CENWAVE setting are of the form:  $FWHM_{\lambda}(\text{''}) = a_0 + a_1*\lambda + a_2*\lambda^2 + \dots a_N*\lambda^N$ , where N is the order of the

polynomial (4<sup>th</sup> order for G130M and G160M and G140L).

| G130M Seg B                                  | A0       | A1       | A2         | A3           | A4           |
|--|----------|----------|------------|--------------|--------------|
| CENWAVE = 1291<br>FPPOS = 4<br>(1136 – 1274) | -6901.46 | 23.6432  | -0.0303313 | 1.72714E-05  | -3.68298E-09 |
| CENWAVE = 1327<br>FPPOS = 1<br>(1179 – 1314) | 21980.70 | -70.3413 | 0.0843730  | -4.49572E-05 | 8.97888E-09  |

| G130M Segment A                              | A0       | A1       | A2        | A3           | A4          |
|--|----------|----------|-----------|--------------|-------------|
| CENWAVE = 1291<br>FPPOS = 4<br>(1292 – 1429) | 52082.70 | -153.772 | 0.170165  | -8.36446E-05 | 1.54093E-08 |
| CENWAVE = 1327<br>FPPOS = 1<br>(1335 – 1470) | 31004.0  | -88.9013 | 0.0955519 | -4.56220E-05 | 8.16419E-09 |

| G160M Segment B                              | A0       | A1      | A2          | A3          | A4           |
|--|----------|---------|-------------|-------------|--------------|
| CENWAVE = 1577<br>FPPOS = 4<br>(1386 – 1556) | -4641.84 | 12.2160 | -0.0120503  | 5.28170E-06 | -8.67910E-10 |
| CENWAVE = 1623<br>FPPOS = 1<br>(1440 -1605)  | -2564.06 | 6.42474 | -0.00603076 | 2.51391E-06 | -3.92660E-10 |

| G160M Segment A                              | A0      | A1       | A2         | A3           | A4          |
|--|---------|----------|------------|--------------|-------------|
| CENWAVE = 1577<br>FPPOS = 4<br>(1578 – 1747) | 3389.70 | -8.43940 | 0.00787035 | -3.25660E-06 | 5.04322E-10 |
| CENWAVE = 1623<br>FPPOS= 1<br>(1632 – 1797)  | 483.795 | -1.49830 | 0.00166764 | -8.00046E-07 | 1.40659E-10 |

| G140L Segment A                              | A0       | A1        | A2           | A3          | A4           |
|--|----------|-----------|--------------|-------------|--------------|
| CENWAVE = 1105<br>FPPOS = 4<br>(1129 – 1864) | -10.4089 | 0.0418745 | -4.79919E-05 | 2.11621E-08 | -2.99988E-12 |
| CENWAVE = 1230<br>FPPOS = 1<br>(1301 – 1868) | 342.668  | -0.86088  | 8.13449E-04  | -3.42109E-7 | 5.40675E-11  |

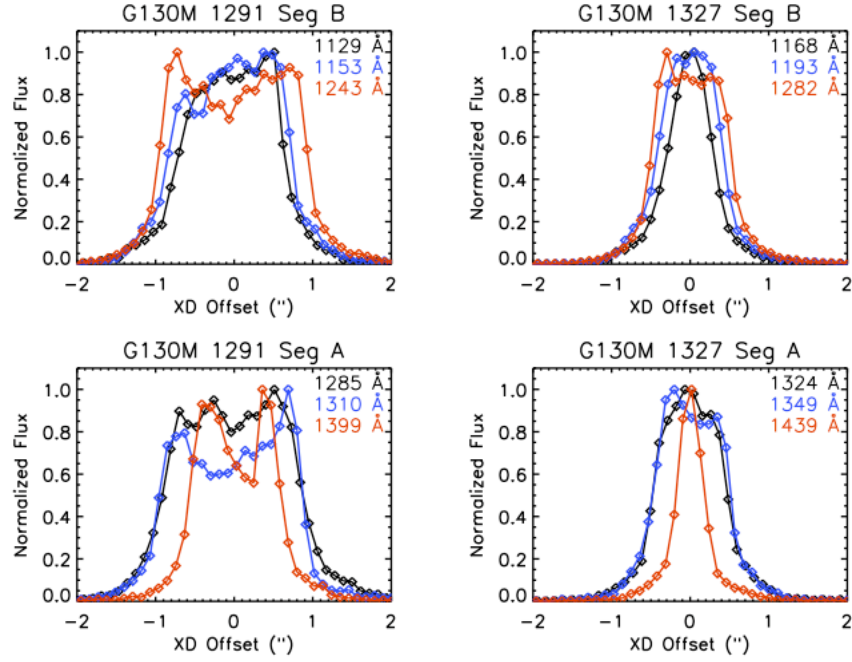


**Figure A1.** Normalized cross-dispersion (spatial) profiles of the G130M PSA spectra of the white dwarf WD0947+857, extracted at selected wavelengths along dispersion. Profiles are shown for Segments A and B, at the shortest and longest central wavelength settings (CENWAVE=1291 and 1327), for the default FPPOS position (=3). A small offset was applied to the latter two profiles in each plot (red and blue), to align them with the first spectrum (black). The shape of the cross-dispersion profile changes significantly with wavelength, ranging from a double-horned profile in the CENWAVE=1291 spectra, to a single profile at the longest wavelengths of the CENWAVE=1327 data. Note the broad wings on the profiles, produced largely by the mid-frequency wavefront errors from the HST OTA.



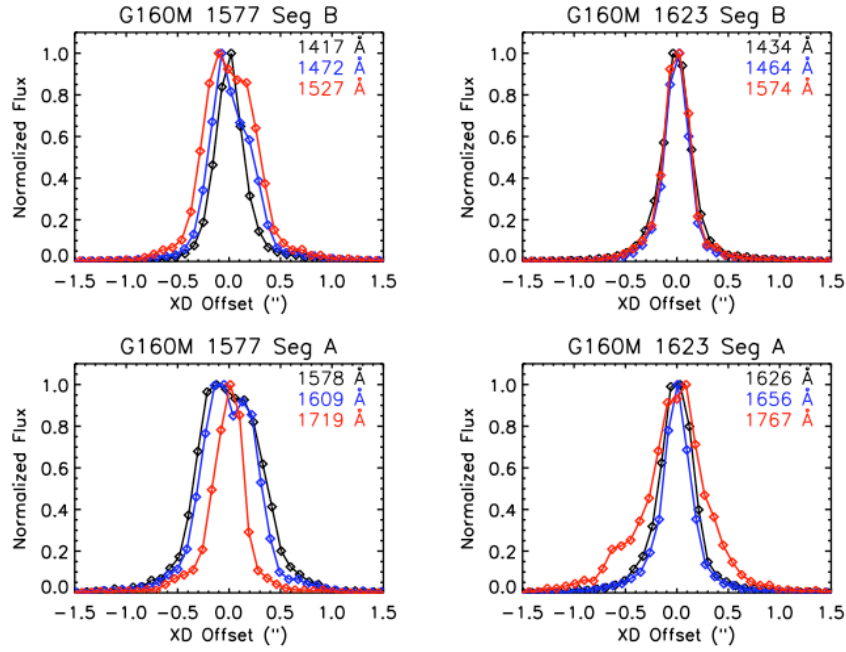


**Figure A2.** Normalized cross-dispersion (spatial) profiles of the G160M PSA spectra of the white dwarf WD1057+719, extracted at selected wavelengths along dispersion. Profiles are shown for Segments A and B, at the shortest and longest central wavelength settings (CENWAVE=1577 and 1623), for the default FPPOS position (=3). A small offset was applied to the latter two profiles in each plot (red and blue), to align them with the first spectrum (black). The profiles are narrower than observed for the G130M spectra (**Figure A1**), reflecting a higher spatial resolution for the G160M spectra. Note the broad wings on the profiles, produced largely by the mid-frequency wavefront errors from the HST OTA.

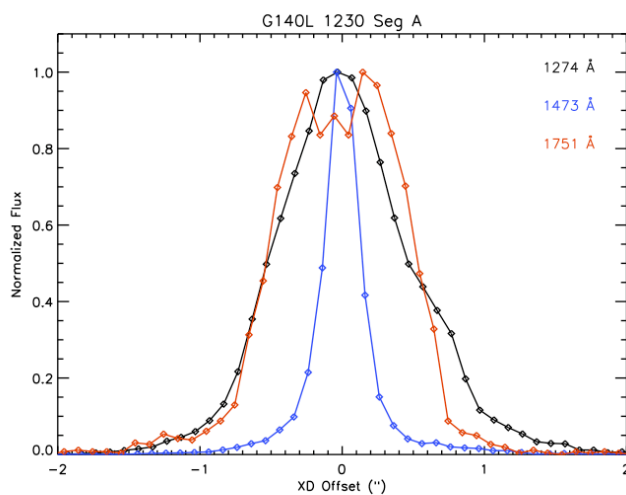


**Figure A3.** Normalized cross-dispersion (spatial) profiles of the G140L PSA spectra of the white dwarf WD0947+857, extracted at selected wavelengths along dispersion. Profiles are shown for Segments A and B, at the CENWAVE=1230 setting, for the default FPPOS position (=3). A small offset was applied to the latter two profiles in each plot (red and blue), to align them with the first spectrum (black). The width of the profile changes significantly with wavelength, starting out broad near 1250 Å, then reaching a minimum near 1450 Å before broadening again at longer wavelengths. Note the broad wings on the profiles, produced largely by the mid-frequency wavefront errors from the HST OTA.

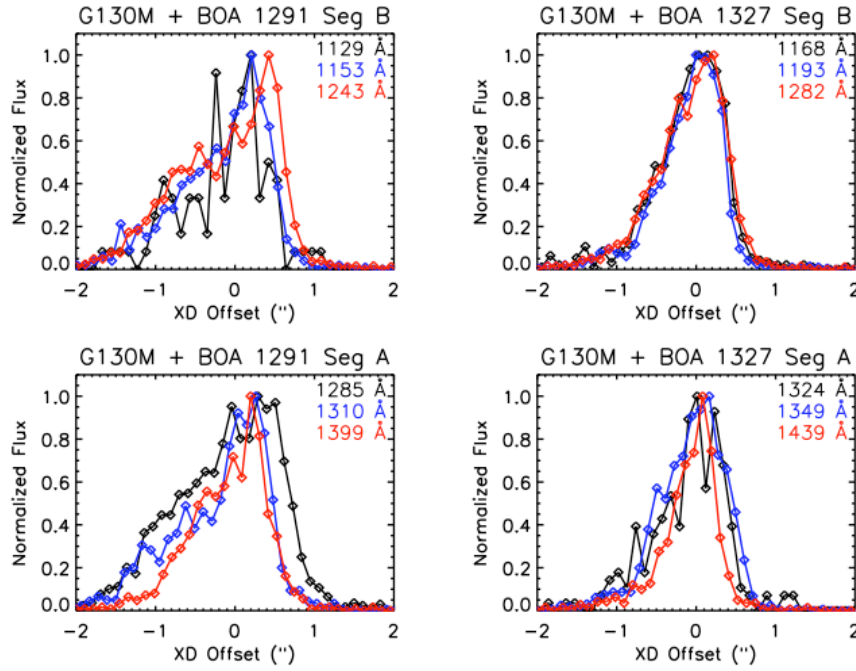


**Figure A4.** Normalized cross-dispersion (spatial) profiles of the G130M BOA spectra of the white dwarf GD71, extracted at selected wavelengths along dispersion. Profiles are shown for Segments A and B, at the shortest and longest central wavelength settings (CENWAVE=1291 and 1327), for FPPOS = 4 and 1, respectively. A small offset was applied to the latter two profiles in each plot (red and blue), to align them with the first spectrum (black). The cross-dispersion profile is strongly asymmetric, with a broad wing extending toward negative offset positions. The wing is produced when the BOA filter wedge induces coma in the image of the target.

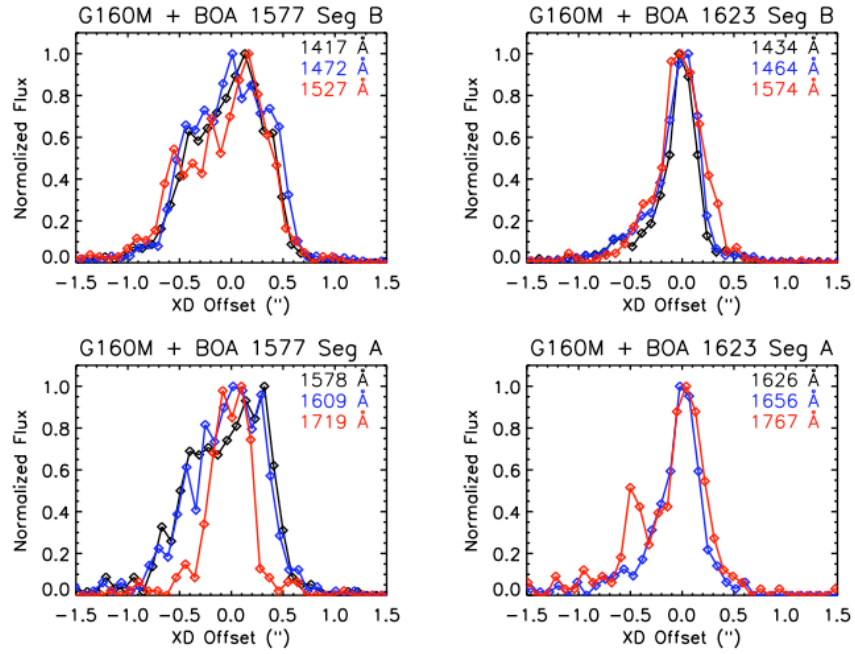


**Figure A5.** Normalized cross-dispersion (spatial) profiles of the G160M BOA spectra of the white dwarf GD71, extracted at selected wavelengths along dispersion. Profiles are shown for Segments A and B, at the shortest and longest central wavelength settings (CENWAVE=1577 and 1623), for FPPOS = 4 and 1, respectively. A small offset was applied to the latter two profiles in each plot (red and blue), to align them with the first spectrum (black). The cross-dispersion profile is strongly asymmetric, with a broad wing extending toward negative offset positions. The wing is produced when the BOA filter wedge induces coma in the image of the target.

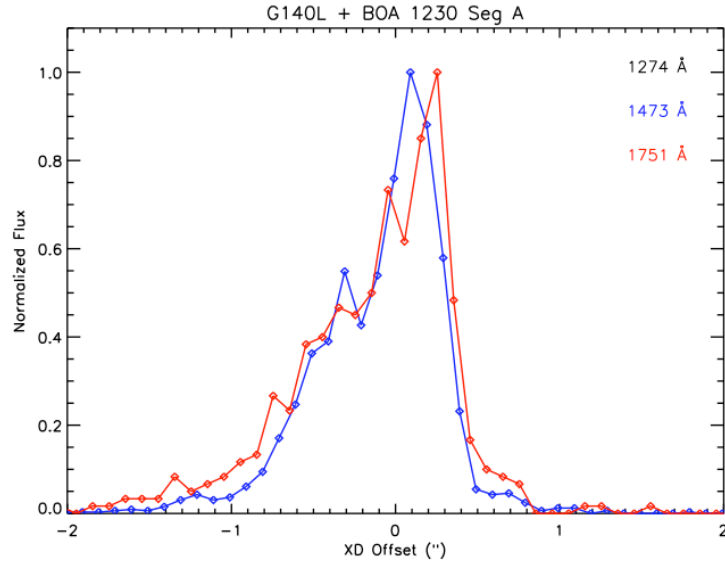


**Figure A6.** Normalized cross-dispersion (spatial) profiles of the G140L BOA spectra of the white dwarf GD71, extracted at selected wavelengths along dispersion. Profiles are shown for the longest central wavelength setting (CENWAVE=1230), for FPPOS = 1. A small offset was applied to the latter two profiles in each plot (red and blue), to align them with the first spectrum (black). The cross-dispersion profile is strongly asymmetric, with a broad wing extending toward negative offset positions. The wing is produced when the BOA filter wedge induces coma in the image of the target.